ACS Catalysis
Research Article
pubs.acs.org/acscatalysis

# $CO_2$ Electroreduction to Hydrocarbons on Carbon-Supported Cu Nanoparticles

Olga A. Baturina,*[†] Qin Lu,[†] Monica A. Padilla,[‡] Le Xin,[§] Wenzhen Li,[§] Alexey Serov,[‡] Kateryna Artyushkova,[‡] Plamen Atanassov,[‡] Feng Xu,[∥,¶] Albert Epshteyn,[†] Todd Brintlinger,[#] Mike Schuette,[⊥] and Greg E. Collins[†]

[†]Chemistry Division and [#]Materials Science and Technology Division, Naval Research Laboratory, Washington, DC 20375, United States

[‡]Department of Chemical and Nuclear Engineering, University of New Mexico, Albuquerque, New Mexico 87131, United States

[§]Department of Chemical and Biological Engineering, Michigan Technological University, Houghton, Michigan 49931, United States

[∥]Wolfson Catalysis Centre, Department of Chemistry, University of Oxford, Oxford OX1 3QR, U.K.

[¶]College of Materials Science and Engineering, Fuzhou University, Fuzhou 350108, China

[⊥]Sotera, Inc, Herndon, Virginia 20171, United States

*Supporting Information*

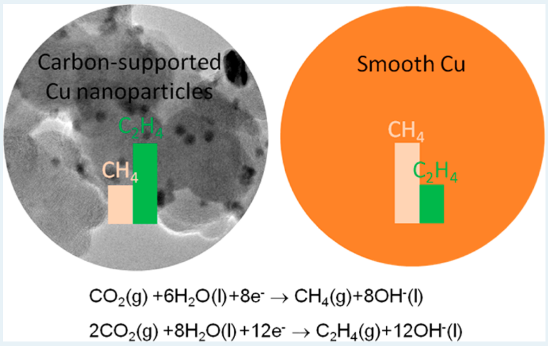

**ABSTRACT:** Activities of Cu nanoparticles supported on carbon black (VC), single-wall carbon nanotubes (SWNTs), and Ketjen Black (KB) toward $CO_2$ electroreduction to hydrocarbons ($CH_4$, $C_2H_2$, $C_2H_4$, and $C_2H_6$) are evaluated using a sealed rotating disk electrode (RDE) setup coupled to a gas chromatograph (GC). Thin films of supported Cu catalysts are deposited on RDE tips following a procedure well-established in the fuel cell community. Lead (Pb) underpotential deposition (UPD) is used to determine the electrochemical surface area (ECSA) of thin films of 40 wt % Cu/VC, 20 wt % Cu/SWNT, 50 wt % Cu/KB, and commercial 20 wt % Cu/VC catalysts on glassy carbon electrodes. Faradaic efficiencies of four carbon-supported Cu catalysts toward $CO_2$ electroreduction to hydrocarbons are compared to that of electrodeposited smooth Cu films. For all the catalysts studied, the only hydrocarbons detected by GC are $CH_4$ and $C_2H_4$. The Cu nanoparticles are found to be more active toward $C_2H_4$ generation versus electrodeposited smooth copper films. For the supported Cu nanocatalysts, the ratio of $C_2H_4/CH_4$ Faradaic efficiencies is believed to be a function of particle size, as higher ratios are observed for smaller Cu nanoparticles. This is likely due to an increase in the fraction of under-coordinated sites, such as corners, edges, and defects, as the nanoparticles become smaller.

**KEYWORDS:** *$CO_2$ electroreduction, rotating disk electrode, Faradaic efficiency, copper nanoparticles, electrocatalytic activity, hydrocarbons, methane, ethylene*

## INTRODUCTION

Carbon dioxide is a greenhouse gas that can be used for production of useful fuels or fuel cell stocks such as methane and ethylene.[1] The electrochemical reduction of carbon dioxide to hydrocarbon fuels is an emerging technology, which has the advantage of being performed under ambient temperature and pressure. As a technology currently in development, it can benefit from accomplishments in the proton exchange membrane fuel cell (PEMFC) technology. The design principles for $CO_2$ electrolyzers are similar to those of PEMFCs in that the catalyst coated proton exchange membrane is used to separate a cathode from an anode and provide catalysts for both reactions. As in the oxygen reduction reaction (ORR), the $CO_2$ reduction reaction at the cathode of a $CO_2$ electrolyzer requires a high-surface-area metal catalyst. At the PEMFC cathode, a high-surface-area metal catalyst is designed by placement of 3−5 nm Pt nanoparticles on a high-surface-area carbon support. Electrocatalytic activities of carbon-supported Pt nanoparticles toward the ORR are typically evaluated in electrochemical cells using a thin-film rotating disk electrode (RDE) method.[2] This method, however, cannot be directly transferred to the $CO_2$ electroreduction reaction. Unlike the ORR, the $CO_2$ electroreduction reaction results in multiple reaction products being generated both in the liquid and gas phase. Depending on the metal catalyst, $CO_2$ electroreduction products may include, but are not limited to, CO, formic acid (HCOOH), alcohols, methane ($CH_4$), and ethylene ($C_2H_4$). The net reactions that occur on metal electrodes in aqueous

**Received:** April 22, 2014
**Revised:** July 21, 2014
**Published:** September 3, 2014

dx.doi.org/10.1021/cs500537y | *ACS Catal.* 2014, 4, 3682−3695

solutions at pH = 0 versus standard hydrogen electrode (SHE) are shown below:

$$CO_2 + 2H^+ + 2e^- \leftrightarrow CO + H_2O, \ E^0 = -0.103 \text{ V} \quad (1)$$

$$CO_2 + 2H^+ + 2e^- \leftrightarrow HCOOH, \ E^0 = -0.225 \text{ V} \quad (2)$$

$$CO_2 + 8H^+ + 8e^- \leftrightarrow CH_4 + 2H_2O, \ E^0 = 0.169 \text{ V} \quad (3)$$

$$2CO_2 + 12H^+ + 12e^- \leftrightarrow C_2H_4 + 4H_2O, \ E^0 = 0.079 \text{ V} \quad (4)$$

$$CO_2 + 6H^+ + 6e^- \leftrightarrow CH_3OH + H_2O, \ E^0 = 0.020 \text{ V} \quad (5)$$

$$2CO_2 + 12H^+ + 12e^- \leftrightarrow C_2H_5OH + 3H_2O, \ E^0 = 0.09 \text{ V} \quad (6)$$

$$2H^+ + 2e^- \leftrightarrow H_2, \ E^0 = 0 \text{ V} \quad (7)$$

$E^0$ in eqs 1−7 represents the standard equilibrium potential.

Although the formation of CO, HCOOH, and alcohols in the course of $CO_2$ electroreduction has been reported for various metals,[3] the only catalyst that selectively generates hydrocarbons ($CH_4$ and $C_2H_4$) with high Faradaic efficiencies is polycrystalline Cu.[1] $CO_2$ electrocatalysis on Cu, however, occurs far from equilibrium and requires ca. 1 V overpotentials.[4,5]

Later studies[5−8] have shown that $CO_2$ electroreduction on Cu was very sensitive to the Cu surface structure. Hori[5,6] demonstrated that Cu(100) facets favored the generation of $C_2H_4$ at less negative potentials versus Cu foil, whereas Cu(111) favored $CH_4$ production at the same potentials. $CO_2$ reduction on Cu(110) facets required the most negative potentials and resulted mostly in the generation of $C_2$ and $C_3$ compounds. High-index crystal facets, such as Cu(311), Cu(511) and Cu(711) tended to be more active toward production of $C_2H_4$ and other $C_2$ and $C_3$ compounds such as ethanol, ethanal, acetic acid, propanal, propanol, and 2-propen-1-ol. The strong dependence of the $CO_2$ reduction product distribution on the Cu surface structure explains the differences in the product distributions for Cu films, electrodeposited under various conditions.[9] For example, Cu electrodeposits that formed honeycomb and 3D foam structures favored production of $C_2H_4$ (13% and 10% Faradaic efficiencies, respectively) and $C_2H_6$ (2% and 6% Faradaic efficiencies, respectively) at −1.9 V versus Ag/AgCl reference electrode, although production of methane was completely suppressed.[8] On the other hand, the Faradaic efficiency for methane (ca. 15%) was higher than for $C_2H_4$ (ca. 8%) on electropolished Cu mesh.[8] Interestingly, a much wider product distribution (up to six carbon atoms in the hydrocarbon chain) was reported for Cu foil that was not pretreated by electropolishing.[10] Detectable quantities of $C_4$−$C_6$ parafins and olefins were identified during electrolysis of $CO_2$-purged 0.1 M $KHCO_3$ solution by Shibata et al.,[10] while holding the untreated Cu electrode at −1.65 V versus Ag/AgCl reference electrode. Total hydrocarbons production was strongly dominated by $C_1$−$C_3$ hydrocarbons (i.e., $CH_4$, $C_2H_4$, $C_2H_6$, and $C_3H_8$). On the basis of early work by others,[11,12] the authors suggested that the oxides on the surface of non-electropolished Cu foil promoted the chain propagation reaction leading to the generation of higher hydrocarbons.[10]

Because the surface of a Cu nanoparticle is a combination of low-index crystal facets and low-coordination sites such as corners, edges, and defects, the distribution of gas phase $CO_2$ reduction products on Cu nanoparticles is expected to be dominated by $C_2$ compounds. The reason for this is that low-coordination sites are reminiscent of stepped surfaces such as Cu(311), Cu(511), and Cu(711) that are more reactive (vs terraces[7]) and selective toward $C_2$ compounds.[5] Indeed, electrodeposited 50−100 nm Cu nanoparticles demonstrated higher selectivity toward $C_2H_4$ production (∼37% Faradaic efficiency) versus that for $CH_4$ (1% Faradaic efficiency) for $CO_2$ electrolysis at −1.1 V versus reversible hydrogen electrode (ca. −1.7 V vs Ag/AgCl) in 0.1 M $KClO_4$ solution.[7]

Carbon-supported Cu nanoparticles have not been extensively explored thus far because of Cu sensitivity to oxidation and experimental difficulties associated with the synthesis of small size nanoparticles. Only a few reports are available in which the activities and selectivities of supported Cu nanoparticles toward the $CO_2$ electroreduction reaction have been evaluated. Cu-doped xerogels with Cu nanoparticles on the order of 50−100 nm were found to be capable of converting $CO_2$ to $C_1$−$C_3$ paraffins and oleffins at −1.65 V versus Ag/AgCl[13], demonstrating a broader product distribution compared to electropolished Cu foil. Product distribution was dominated by $CH_4$ (∼50% selectivity) over $C_2$ (∼24% selectivity) and $C_3$ (∼27% selectivity) compounds. Because product distribution was not presented in terms of Faradaic efficiencies in ref 13, it is impossible to compare the results obtained on supported nanoparticles to the ones on electropolished Cu foil and unsupported nanoparticles. Other dopants such as Fe and Ni also promoted C−C bond formation.[13] $C_1$−$C_3$ and $C_1$−$C_4$ paraffins and olefins were detected on Fe- and Ni-doped xerogels, respectively, at −1.65 V versus Ag/AgCl. However, total Faradaic efficiency for hydrocarbons generation at Ni-doped xerogel was extremely low (1.5%).[13]

Activities and selectivities of carbon-supported transition and noble metal catalysts toward $CO_2$ electroreduction were found to be significantly different at the triple phase boundary versus those at the electrode/solution interface.[14,15] While carbon-nanotube (CNT) supported Fe and Pt nanoparticles demonstrated activity toward $C_1$−$C_3$ compounds generation at the triple phase boundary, their foils were inactive toward hydrocarbons generation at the electrode/solution interface.[1] Product distribution at the triple phase boundary, however, was strongly dominated by $H_2$ and CO (ca. 99% Faradaic efficiency for $H_2$ + CO) for both CNT-supported Fe and Pt catalysts at 60 °C and −1.4 V versus Ag/AgCl. Total Faradaic efficiency for $C_1$−$C_3$ generation (including reaction products both in liquid and gas phase) accounted for ca. 0.5%. Regarding the $C_1$−$C_3$ formation, Cu/CNT performed worse than CNT-supported Pt and Fe, contrary to the superior activity of Cu foil at the electrode/solution interface.[14]

The majority of experimental[4,16−20] and theoretical[21] studies of the kinetics and the mechanism of $CO_2$ reduction to $CH_4$ (eq 3) and $C_2H_4$ (eq 4) were carried out on polycrystalline Cu. Both reactions were demonstrated to be kinetically limited, and CO was identified as the key intermediate in the production of hydrocarbons. Recent theoretical analysis by Peterson and Norskov[22] suggests that the limiting reaction step involves the hydrogenation of CO to CHO, similar to the gas-phase $CO_2$ hydrogenation. The kinetics of $CO_2$ electroreduction, in particular, was studied using a RDE method, which is traditionally used to study reactions that occur under mixed kinetic−diffusion control.[23,24] Analysis of reaction products in these papers was solely focused on the liquid phase, either by gas chromatography (GC) from liquid injection or electrochemically[25] by the oxidation of reaction products at the ring surrounding the disk electrode (rotating ring disk electrode method, RRDE).

Here we combine GC analysis of $CO_2$ electroreduction products at the electrode/solution interface with the thin-film RDE method in order to compare the activities and selectivities of 10−30 nm supported Cu nanoparticles to that of the smooth electrodeposited Cu films with respect to $CO_2$ electroreduction to hydrocarbons. Nanoscale Cu catalysts supported on conventional supports (VC, KB) and nanostructured SWNTs are synthesized and characterized by X-ray diffraction (XRD) analysis, high-resolution transmission electron microscopy (HRTEM), X-ray photoelectron spectroscopy (XPS) and Pb underpotential deposition (UPD)[26,27] to obtain information on particle size, speciation, morphology, and electrochemically accessible surface area (ECSA). Thin films of supported Cu catalysts are deposited on the surface of glassy carbon disks, and their Faradaic efficiencies toward $CO_2$ electroreduction are evaluated under potentiostatic conditions. Although liquid reaction products can be analyzed with high accuracy using liquid-phase nuclear magnetic resonance analysis,[28−31] the scope of this investigation was restricted to gas phase reaction products.

## ■ EXPERIMENTAL SECTION

**Materials.** Ultrahigh purity $KHCO_3$ (Sigma-Aldrich), ACS grade $Pb(ClO_4)_2$ (Sigma-Aldrich), ACS grade $CuSO_4{\cdot}5H_2O$ (Sigma-Aldrich), double-distilled $H_2SO_4$ (Veritas), and Nanopure water (Millipore, 18.2 MΩ cm, 4 ppb total organic carbon) were used for preparation of solutions. Twenty wt % Cu catalyst supported on Vulcan Carbon XC72R (VC) was purchased from Premetek, Inc.

**Synthesis.** Catalysts were synthesized using three different synthetic routes: (1) a nanocapsule method[32] with $LiBEt_3H$ as the reducing agent, (2) a hydrazine method using $N_2H_4$ as the reducing agent, and (3) an ethylene glycol method with $NaBH_4$ as the reducing agent. Vulcan carbon XC72R, Ketjen black (KB), and single-wall nanotubes (SWNTs) were used as catalyst supports in methods 1−3, respectively.

*(1). Synthesis of 40 wt % Cu/VC.* A suspension of 48 mg of VC (Vulcan XC-72R) in a mixture of 15 mL of oleylamine and 20 mL of hexane was prepared at room temperature and sonicated in an ultrasound sonicator (Branson 2510) for 1 h. The mixture was heated to 90 °C and held for 1 h under $N_2$ flow until the hexane evaporated. After cooling down to 80 °C, 0.5 mmol of fully dissolved $Cu(acac)_2$ (copper(II) acelylacetonate) in a mixture of 5 mL oleylamine and 0.32 mL of oleic acid was added. The reactive mixture was heated to 120 °C, and a quick injection of 1.5 mL of 1 M $LiBEt_3H$ in THF followed. The solution was further held for 1 h under a $N_2$ blanket and cooled down to room temperature. The 40 wt % Cu/VC catalyst was collected by filtration, washing with copious amounts of $N_2$-purged ethanol and then dried in vacuum oven at room temperature overnight.

*(2). Synthesis of 50 wt % Cu/KB.* A 50 wt % Cu/KB catalyst was synthesized in a three-step process. First, one-third of the initially calculated amount of copper nitrate (ACS reagent, Sigma-Aldrich) was dissolved in ethanol, and KB 600J (Akzo Nobel) was introduced into solution. The black slurry was agitated using an utrasound bath for 30 min. Then, an excess amount of 20 wt % $N_2H_4$ in water was added to the slurry dropwise under vigorous stirring. After the solvents evaporated at 85 °C overnight, the dry composite material was ground with an agate mortar and pestle. The fine powder was transferred into a tube furnace and heat treated in a flow of nitrogen at 250 °C for 1 h. Seventeen wt % Cu/KB was obtained as a final product of the first step. The next two steps were a reproduction of the first step, with 17 wt % Cu/KB and 34 wt % Cu/KB as starting materials, respectively. A final heat treatment was performed in a reductive atmosphere of hydrogen (7 vol % in $N_2$) at 250 °C for 2 h. The nitrogen and hydrogen flow rates were 100 mL $min^{-1}$. A three - step deposition process, with ca. 17 wt % of copper deposited at every step, is thought to prevent growth and agglomeration of Cu nanoparticles.

*(3). Synthesis of 20 wt % Cu/SWNT.* Raw chemical vapor deposition (CVD) SWNTs were supplied by Thomas Swan & Co Ltd. As obtained, SWNTs were first treated by $H_2O$ steam at 900 °C for 4 h to remove amorphous carbon.[33] After steam purification, the sample was mixed with 6 M HCl and the mixture was refluxed for 2 h to remove any metal particles. Prior to synthesis of SWNT-supported Cu nanoparticles, SWNTs (80 mg) were dispersed in aqueous ethylene glycol solution (20% v/v) by sonication for 1 h. $CuCl_2$ $2H_2O$ (53.69 mg) was added to this dispersion and the mixture was stirred overnight under $N_2$. The flask containing the mixture was placed in an ice bath before adding a freshly made $NaBH_4$ solution (100 mg $NaBH_4$ in 5 mL $H_2O$). The flask was kept in an ice bath for another 2 h under $N_2$ to ensure the complete reduction of $Cu^{2+}$ to $Cu^0$. The Cu nanoparticles supported on SWNTs (20 wt %) were collected by filtering the mixture through a Nylon membrane (0.2 $\mu$m).

Prior to electrochemical or microscopic characterization, all supported Cu catalysts were reduced in a tube furnace in a flow of 10 vol % $H_2$ (Air Liquide, 99.999%) in UHP Ar (Air Liquide, 99.999%) at 250 °C for 2 h at a flow rate of 50 mL $min^{-1}$. For electrochemical characterization, VC, KB and SWNT supports were reduced in $H_2$ in the same manner, as the supported Cu catalysts.

**Cu Electrodeposition.** Cu electrodeposition on Pt disk electrodes (Pine Instruments, 5 mm diameter) was carried out in degassed solutions of 0.5 M $H_2SO_4$ + 0.05 M $CuSO_4$. The potential of the Pt disk electrode, spinning at 1600 rpm, was cycled between −0.6 and 1.0 V three times at 50 mV $s^{-1}$ prior to the final scan from 1.0 to −0.6 V, in which the Cu film was deposited. Pt disk electrodes were polished and cleaned ultrasonically, for 4 min in nanopure water prior to mounting in the RDE setup. The thickness of the Cu films, determined from the charge released during Cu stripping from the Pt disk electrode in 0.5 M $H_2SO_4$ solution, was 370 ± 10 nm. The calculations assumed $2e^-$ transferred for $Cu^0$ dissolution to $Cu^{2+}$ and a Cu density of 8.93 g $cm^{-3}$.

X-ray diffraction (XRD), X-ray photoelectron spectroscopy (XPS), and high-resolution transmission electron microscopy (HRTEM) were used for nanoparticle ex situ analysis.

**XRD.** The phase composition and Cu particle size in the supported Cu catalysts were determined from XRD patterns. The XRD spectra were acquired using a Rigaku SmartLab X-ray diffractometer in PB geometry equipped with a Cu K$\alpha$ radiation source and a D-teX linear Si detector.

**XPS.** XPS measurements were performed with a Kratos Axis Ultra DLD X-ray photoelectron spectrometer using a monochromatic Al K$\alpha$ source operating at 225 W. The data obtained are the average of three different areas per sample. High-resolution C 1s, O 1s, and Cu 2p spectra were acquired. No charge compensation was necessary.

**HRTEM.** Copper nanoparticles on different supports were dispersed by ultrasonic sonication (Branson 2510) in glass vials containing 2.5 mL of ethanol prior to depositing them on copper-supported lacey carbon TEM grids (TedPella, Inc.). Supported Cu nanoparticles were examined by HRTEM using a JEOL JEM 2200 FS transmission electron microscope equipped with an Ultrascan Orius 1000 CCD camera and an Oxford energy dispersive spectroscopy (EDS) system. Micrographs were obtained in bright-field and high-angle annular dark field modes.

**RDE Coupled to GC.** A sealed RDE setup was designed in order to analyze the $CO_2$ electroreduction products. To seal the connection between the standard three-electrode electrochemical cell and the shaft of the rotator (AFCPRB, Pine Instruments), a gas-purging bearing assembly (Pine Instruments, 15 mm diameter) was modified by an in-house bearing assembly with an O-ring inserted into the groove at the top of the assembly. The modified gas-purging assembly was mounted into the large neck of the five-neck electrochemical cell (200 mL, Pine Instruments) and connected to a sampling port of gas chromatograph (Bruker 450-GC) by the PTFE tubing (2 mm outer diameter). Large surface area custom-made RDE disks (Pine Instruments, 7 mm diameter) were used as supports for thin films of supported Cu catalysts. Large surface area working electrodes were employed in order to increase the signal-to-noise ratio for gas-phase GC analysis. Pt foil and Ag/AgCl electrode in 3 M KCl (BASi, 0.22 V vs SHE) served as the counter and reference electrode, respectively. Both electrodes were immersed in 12 mm glass tubes (Pine Instruments, 14/20 sleeve) with glass frits at the end, in order to avoid electrodes' direct contact with solution in the cell. When assembled, the cell was moved up to the shaft of the rotator, so that the top of the modified bearing assembly was in tight contact with the bottom of the shaft. The cell was fixed in this position. Careful attention was paid to a proper sealing of all the junctions in the cell. Teflon tape was applied to ensure the sealing of the cell, if $CO_2$ did not flow freely from the cell outlet.

An electrochemical cell filled with 150 mL of 0.1 M $KHCO_3$ was purged for 30 min with $CO_2$ (Scott Specialty Gases, 99.997%, SFE grade) flowing at 60 mL $min^{-1}$ before the RDE thin-film working electrode was immersed in the cell. The $CO_2$ did not contain any traces of organic impurities, as confirmed by GC analysis. Immediately after mounting the RDE electrode in the cell, a potential of −0.4 V was applied to prevent oxidation of the Cu catalyst. The electrode was pretreated at −0.4 V for 20 min in the $CO_2$-saturated solution before potentiostatic or potentiodynamic measurements were implemented. The gas mixture flowing through the electrochemical cell was sampled every 5, 25, 45, and 65 min. All potentials are given with respect to Ag/AgCl reference electrode.

**Preparation of Thin-Film Electrodes for RDE Experiments.** The catalyst inks were prepared by dispersing an appropriate amount of the freshly reduced, supported Cu catalysts in 5 mL of $O_2$-free isopropanol containing 0.002 vol % of 5 wt % Nafion ionomer (Ion Power, Liquion 1100). The amount of Cu in each ink was fixed at 0.4 $mg_{Cu}$/ml, regardless of the Cu loading on the support. The ink was sonicated for 30 min and left to stir overnight. A glassy carbon RDE that served as a working electrode was used as a substrate for the supported catalysts. A cleaning procedure for RDE electrodes with glassy carbon tips is described elsewhere.[2,34] Briefly, the electrode was polished with a 0.03 $\mu$m alumina particle suspension (Buehler) for 2 min, rinsed with copious amount of nanopure water, washed in an ultrasonic bath for 4 min, and then placed to dry in a small homemade laminar flow hood under Ar. A 19.6 $\mu$L aliquot of well-dispersed catalyst ink was deposited on the surface of a dry glassy carbon electrode. High-quality thin films were formed by drying the inks under a stream of UHP Ar (Air Liquide, 99.999%), preventing oxidation of the Cu nanoparticles.

**Evaluation of Cu Electrochemical Surface Area (ECSA).** ECSA measurements of electrodeposited Cu and supported Cu nanoparticles were carried out by Pb underpotential deposition (UPD)[26,27,35] from a solution of 0.1 M $HClO_4$ + 0.001 M $Pb(ClO_4)_2$. Pt or glassy carbon disks (Pine Instruments, 5 mm diameter) coated with a film of electrodeposited Cu or supported Cu nanoparticles, respectively, were immersed in a degassed 0.1 M $HClO_4$ solution and held at −0.375 V versus Ag/AgCl for 10 min before a background potentiodynamic scan was recorded between −0.375 and −0.110 V at 10 $mVs.^{-1}$. A stock solution of $Pb(ClO_4)_2$ in $HClO_4$ was used to introduce 1 mM $Pb(ClO_4)_2$ into the cell with continual rotation of the electrode at 1600 rpm. Subsequently, the electrode was held at −0.375 V for 10 min prior to the stripping of Pb by sweeping the potential from −0.375 to −0.05 V at 10 $mVs.^{-1}$. The charge consumed for the oxidation of Pb adatoms was determined by integrating the current versus time curve, which was obtained by subtracting the background current (measured in the absence of $Pb(ClO_4)_2$) from the current measured in the presence of 1 mM $Pb(ClO_4)_2$. Integration limits were −0.375 and −0.05 V for electrodeposited Cu, −0.35 and −0.15 V for 40 wt % Cu/VC, 20 wt % Cu/SWNT and 50 wt % Cu/KB, and −0.35 and −0.2 V for commercial 20 wt % Cu/VC. The Cu ECSA calculations assume a monolayer of Pb adatoms coverage over Cu and $2e^-$ Pb oxidation with a conversion factor of 310 $\mu C\ cm^{-2}$.[27] Each experiment was repeated at least three times, and the average of three ECSAs measurements is reported here. We assume for all further analysis that the same Cu sites that are accessible for Pb UPD in 0.1 M $HClO_4$ + 0.001 M $Pb(ClO_4)_2$ are also accessible for adsorption of $CO_2$ molecules in 0.1 M $KHCO_3$ at pH = 6.8. Ideally, the Cu ECSA would be directly measured in a solution of 0.1 M $KHCO_3$ at pH = 6.8, but to the best of our knowledge, no method has been developed to do so in neutral solutions.

**Online GC Analysis of $CO_2$ Electroreduction Products in Gas Phase.** The gas chromatograph (Bruker 450-GC) was equipped with a custom-made outlet port that was used for online analysis of the effluent gas from the electrochemical cell. Thermal conductivity (TCD) and flame ionization detectors (FID) were capable of quantifying $H_2$, $N_2$, $O_2$, CO, $CO_2$, $CH_4$, $C_2H_2$, $C_2H_4$, and $C_2H_6$ in the outlet stream. Detection of CO and $CO_2$ by the FID detector was achieved using a catalytic methanizer (Bruker). Three columns were used to separate gases before their analysis: Haysep P 80/100, Carboxen 1000 60/80 and Molsieve 13X 80/100. The volume of the GC sample loop was 0.5 mL. The sample loop was purged for 5 min by the gases exiting the electrochemical cell before initiating GC measurements. The GC analysis of the effluent gas required 15 min.

Faradaic efficiencies were calculated as ratios of partial currents for production of particular products ($H_2$, CO, $CH_4$, and $C_2H_4$) to total current measured when constant potential was applied. Partial currents were calculated using Faraday's law and calibration constants obtained by running calibration mixtures containing (1) 10 ppm of CO, $CH_4$, $C_2H_2$, $C_2H_4$, $C_2H_6$, 100 ppm of $H_2$, 100 ppm of $N_2$ and $O_2$ in balance Ar and

Table 1. Cu Particle Size and Cu ECSAs Determined by Pb UPD and Calculated Assuming Spherical Cu Nanoparticles with XRD-Based Diameter

| | particle diameter by XRD (nm) | particle diameter by TEM (nm) | Cu ECSA by Pb UPD ($m^2\ g_{Cu}^{-1}$) | theoretical SA with XRD-based diameters ($m^2\ g_{Cu}^{-1}$) | roughness factor |
|---|---|---|---|---|---|
| 40 wt % Cu/VC | 12 ± 1 | 8−13 | 6.4 ± 0.8 | 55.9 | |
| 20 wt % Cu/SWNT | 19 ± 2 | 15−25 | 2.8 ± 0.2 | 35.2 | |
| 50 wt % Cu/KB | 24 ± 2 | 70−80 | 2.7 ± 0.3 | 28.0 | |
| 20 wt % Cu/VC, Premetek | 27 ± 2 | 70−130 | 0.70 ± 0.07 | 24.9 | |
| electrodeposited Cu | | | | | 1.02 ± 0.10 |

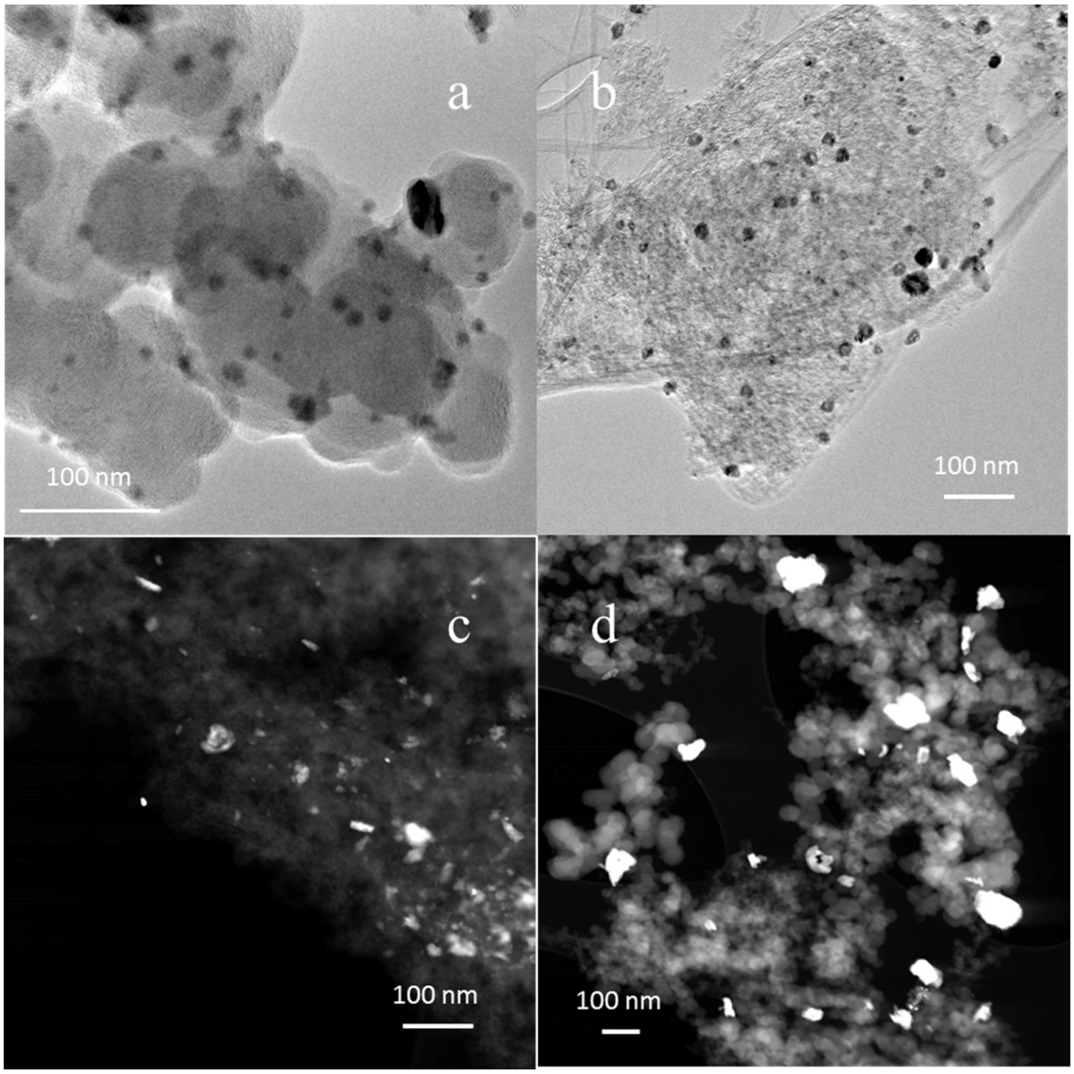

Figure 1. HRTEM bright-field images of (a) 40 wt % Cu/VC and (b) 20 wt % Cu/SWNT, and dark-field images of (c) 50 wt % Cu/KB and (d) 20 wt % Cu/VC.

(2) 100 ppm of CO, $CH_4$, $C_2H_2$, $C_2H_4$, $C_2H_6$, 1000 ppm of $H_2$, $N_2$ and $O_2$ in a balance Ar.

## RESULTS AND DISCUSSION

Prior to the evaluation of electrocatalytic activity for $CO_2$ electroreduction, the supported Cu catalysts were characterized by XPS, XRD, and HRTEM to determine the Cu nanoparticles surface composition, crystal structure, particle size, and morphology. XPS analysis showed that the surfaces of Cu nanoparticles were completely oxidized before the $H_2$-reduction step for all the samples, except 20 wt % Cu/SWNT (see Table S1). This sample had both metallic (42.2%) and oxidized (57.8%) Cu present. Following $H_2$-reduction, oxidized Cu is completely reduced to $Cu^0$ in all four samples. After reductive treatment in $H_2$, the oxygen content decreases for all the samples, except commercial 20 wt % Cu/VC, and varies between 3.0% for 50 wt % Cu/KB and 9.3% for 40 wt % Cu/VC. This remaining oxygen originates from functional groups bound to carbon supports. Reduction by $H_2$ leads to the highest degree of reduction as manifested by a significant increase in the relative amount of overall carbon and, more particularly, graphitic carbon for the high Cu loading samples (40 wt % Cu/VC and 50 wt % Cu/KB). However, the highest amount of graphitic carbon both before and after $H_2$-reduction was observed for the SWNT support (56.1 and 58.5%, respectively). Overall, 20 wt % Cu/SWNT catalyst showed the highest stability during the $H_2$-treatment, as both total elemental composition and Cu/C ratio did not change significantly before and after the reductive treatment.

XRD patterns were strongly dominated by (111), (200), and (220) Cu metal crystal planes for the four catalysts. A negligible amount of surface oxide generated on the Cu nanoparticle surface after exposure to air, was reduced electrochemically while holding the thin-film electrode at −0.4 V for 20 min in a $CO_2$-purged solution of 0.1 M $KHCO_3$. Particle sizes determined from Sherrer's equation and HRTEM images for 40 wt % Cu/VC, 20 wt % Cu/SWNT, 50 wt % Cu/KB, and commercial 20 wt % Cu/VC catalyst (Premetek, Inc.) are compared in Table 1. The average Cu particle size is 12 nm (second column) for the 40 wt % Cu/VC nanocapsule catalyst, although it falls within the 19−27 nm range for the three remaining catalysts. Particle size analysis by XRD is usually complemented by HRTEM in order to visualize nanoparticles and obtain information on the particle size distribution and their dispersion on the surface of the support. HRTEM images of the three homemade Cu catalysts and the commercial 20 wt % Cu/VC are shown in Figure 1a−d. The micrographs shown in Figure 1 reveal that the Cu nanoparticles from 40 wt % Cu/VC (Figure 1a) and 20 wt % Cu/SWNT (Figure 1b) are uniformly distributed and well-dispersed, whereas the Cu particles from the two other catalysts, 50% Cu/KB (Figure 1c) and 20% Cu/VC (Figure 1d), are not as uniformly distributed on the supports and are more agglomerated. Most of the Cu nanoparticles from the 40 wt % Cu/VC sample in Figure 1a are within the 8−13 nm range, although the size of Cu nanoparticles from the 20 wt % Cu/SWNT catalyst (Figure 1b) falls within 15−25 nm. The diameter of Cu nanoparticles derived from the XRD spectra for 40 wt % Cu/VC (12 nm) and 20 wt % Cu/SWNT (19 nm) catalysts falls within the range realized from the TEM images, shown in Figure 1a,b, respectively. On the contrary, for 50 wt % Cu/KB and commercial 20 wt % Cu/VC, the range of diameters for Cu nanoparticles from the TEM images (Figure 1c,d, respectively) deviates significantly from the values derived from XRD patterns. Cu particles on the order of 70−80 nm and 70−130 nm can be seen for the 50 wt % Cu/KB and 20 wt % Cu/VC catalysts, respectively, while their XRD-based diameters are 24 and 27 nm (Column 2, Table 1). This is likely due to the agglomeration of Cu nanoparticles. Higher agglomeration of 20 wt % Cu/VC and 50 wt % Cu/KB is indirectly confirmed by XPS (Column 5, Table S1), as both samples have the lowest Cu/C ratio (0.001). On the contrary, better dispersion of 40 wt % Cu/VC and 20 wt % Cu/SWNT is evidenced by a much higher Cu/C ratio of 0.02. In addition, Cu nanoparticles in 20 wt % Cu/SWNT catalyst are the least subject to agglomeration, as their Cu/C ratio does not change following the heat-treatment in $H_2$, contrary to other samples.

High agglomeration of 50 wt % Cu/KB catalyst is likely due to its high metal loading. Although it is feasible to synthesize well-dispersed carbon-supported Pt catalysts at such high metal loading, it is significantly more challenging for supported Cu catalysts. Because the density of Cu (8.93 g $cm^{-3}$) is a factor of 2.3 lower than the density of Pt (21.4 g $cm^{-3}$), the number of same size Cu nanoparticles per unit surface area at the same mass loading will be a factor of 2.3 versus the number of Pt nanoparticles. The closer the nanoparticles are to each other on the support surface, the more likely they will agglomerate, especially when thermal treatment ($H_2$-reduction at 250 °C) is involved. Although we cannot comment on the reasons for high agglomeration of commercial 20 wt % Cu/VC, we noticed that using aqueous media during the synthesis of Cu nanoparticles usually results in a larger Cu particle size and higher agglomeration of Cu nanoparticles.

The ECSAs of Cu nanoparticles and electrodeposited Cu films were determined by Pb UPD from 0.1 M $HClO_4$ + 0.001 M $Pb(ClO_4)_2$ solutions.[35] Adsorption of foreign metal atoms is an alternative to traditional methods of ECSA evaluation in catalysts, such as hydrogen UPD or CO stripping on Pt.[35] Previously, we used Cu UPD to determine Pt ECSA for thin films of Pt/VC and $Pt_3Co$/VC catalysts, and obtained consistent results among the three methods.[36] Similar to Cu UPD, Pb UPD is also used for ECSA determination of polycrystalline Pt.[37] Prior to using Pb UPD to determine Cu electrochemical surface area, the feasibility of Pb UPD on Pt/VC thin films was confirmed by comparison of the Pt ECSA determined by Pb UPD to the ECSA obtained by hydrogen UPD. The results by both methods for thin films of 20 wt % Pt/VC (BASF) were in good agreement.

Figure 2 shows current ($I$) versus potential ($E$) curves for Pb stripping (solid lines) from four carbon-supported Cu catalysts (Figure 2a−d) and electrodeposited Cu films (Figure 2e). Electrodeposited Cu films were used as a reference. All the Pb-stripping curves shown in Figure 2 (solid curves) demonstrate a broad peak at −0.25 V due to Pb electrochemical desorption from the Cu surface. Cu ECSA calculated from the charge consumed for stripping the Pb monolayer from the Cu surface falls within the 0.7−6.4 $m^2\ g_{Cu}^{-1}$ range (Column 4, Table 1). The highest ECSA of 6.4 ± 0.8 $m^2\ g_{Cu}^{-1}$ was obtained for 12 nm nanocapsule 20 wt % Cu/VC catalysts, and the lowest one (0.7 ± 0.07 $m^2\ g_{Cu}^{-1}$) for the commercial 20 wt % Cu/VC (27

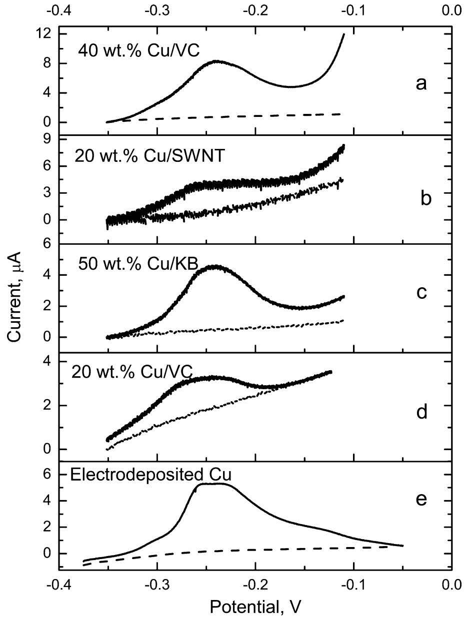

**Figure 2.** Solid curves—Pb stripping from thin films of (a) 40 wt % Cu/VC, (b) 20 wt % Cu/SWNT, (c) 50 wt % Cu/KB, (d) 20 wt % Cu/VC, and (e) electrodeposited Cu in $O_2$-free 0.001 M $Pb(ClO_4)_2$ + 0.1 M $HClO_4$ aqueous solution. Dashed curves—background in $O_2$-free 0.1 M $HClO_4$ solution, 10 mV $s^{-1}$ scan rate, initial potential hold at −0.375 V for 10 min.

nm Cu particle size). The trend in the changes of the Cu ECSA is consistent with an increase in Cu particle size and level of agglomeration of Cu nanoparticles. A comparison of the theoretical Cu surface area calculated assuming a spherical shape with XRD-based diameter for Cu nanoparticles (Column 5, Table 1) to experimental Cu ECSA (Column 4, Table 1) indicates low Cu utilization (ratio of experimental Cu ECSA to the theoretical one expressed in %) in all supported catalysts. For example, the Cu utilization for 20 wt % Cu/VC is ~3% (Cu ECSA is 0.7 ± 0.07 $m^2\ g_{Cu}^{-1}$, and the theoretical surface area is 24.9 $m^2\ g_{Cu}^{-1}$). The Cu utilization is higher for the three homemade catalysts (~10%). This low utilization is likely due to the agglomeration of Cu nanoparticles which is difficult to avoid even for relatively low (20 wt %) Cu loadings.

The ECSA of electrodeposited Cu films as measured by Pb UPD (Figure 2e) is 0.20 ± 0.02 $cm^2$, which is close to a geometric surface area of the Pt disk electrode of 0.196 $cm^2$. This gives a roughness factor (ratio of ECSA to a geometric surface area) of 1.02 ± 0.10 (Column 6, Table 1), implying that these electrodeposited Cu films have a smooth surface, reminiscent of a polished mirror finish Pt disk.

The $CO_2$ electroreduction reaction on Cu thin-film RDE electrodes made from supported Cu catalysts is compared to that of electrodeposited Cu in Figure 3. Interestingly, the shape of current versus potential curves shown in Figure 3 is different from the sigmoidal shape typically observed for the electrochemical process that reaches a purely diffusion controlled state (e.g., the ORR on Pt [2]). The initial current increase for the $CO_2$ electroreduction reaction is not followed by a current plateau. Instead, a monotonic increase in the cathodic current as the potential becomes more negative is followed by a short (ca. 30 mV) potential region in which the current remains constant. Following this region, the cathodic current increases monotonically, again. This is due to the hydrogen evolution reaction (HER) that occurs in parallel with the $CO_2$ electroreduction reaction. The former masks the limiting diffusion current for $CO_2$ electroreduction. The short current plateaus are observed between −1.25 and −1.30 V for all the catalysts except for the commercial 20 wt % Cu/VC (black curve in Figure 3). The onset potential for current plateaus is shifted positively by 30 mV for 50 wt % Cu/KB and 40 wt % Cu/VC versus electrodeposited Cu (−1.25 V vs −1.28 V). For the 20% Cu/SWNT catalyst, the current plateau starts at −1.27 V. Similar current plateaus were reported by other researchers on polycrystalline Cu electrodes.[1,4] Hori[4] observed a shoulder with an inflection point near −1.01 V versus SHE in $CO_2$ reduction voltammograms measured in $CO_2$-saturated 0.1 M $KHCO_3$ solutions. Considering that the current to the right of the shoulder is mostly due to hydrogen evolution,[38] the shoulder was assigned by Hori[4,39] to inhibition of hydrogen evolution by a monolayer of adsorbed CO, the product of the $CO_2$ electroreduction reaction in this potential region (−0.8 to −1.5 V vs SHE). The shoulder shape and position strongly depends on pH,[39] Cu crystal orientation[39] and electrolyte composition.[4,38,39] The possible reasons behind the presence and absence of the shoulder for different samples in Figure 3 will be discussed later.

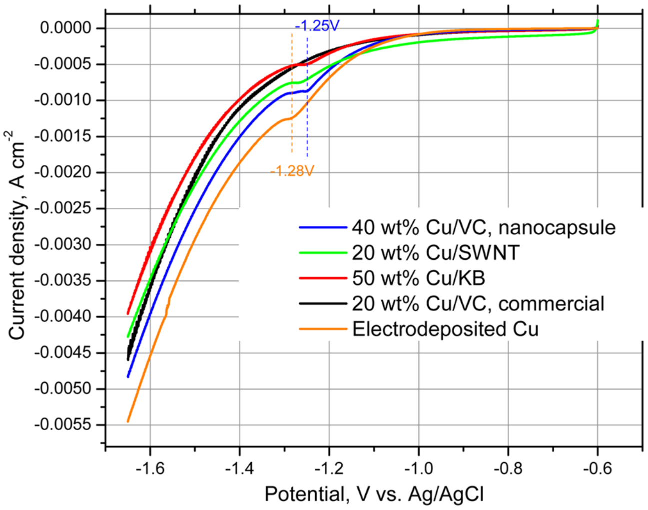

**Figure 3.** Current densities (per geometric surface area) vs potential for $CO_2$ electroreduction at thin films of 40 wt % Cu/VC (blue), 20 wt % Cu/SWNT (green), 50 wt % Cu/KB (red), 20 wt % Cu/VC (black), and electrodeposited Cu (orange) in $CO_2$-purged 0.1 M $KHCO_3$ solution, 1600 rpm, 20 mV $s^{-1}$, pH = 6.8. Only cathodic scans are shown.

In the low potential region (between −0.6 and −1.1 V), preceding the onset potential for $CO_2$ reduction, a higher cathodic current is observed for 20 wt % Cu/SWNT catalyst. This is likely due to a higher capacitive current for the SWNT support.

In order to quantify the gas-phase reaction products on carbon-supported Cu catalysts and electrodeposited Cu, current versus time curves were recorded at −1.2, −1.4, −1.6, −1.8, −2.0, and −2.2 V in an electrochemical cell connected to a gas chromatograph. A representative series of curves measured at −1.2, −1.6, and −2.2 V are shown in Figure 4.

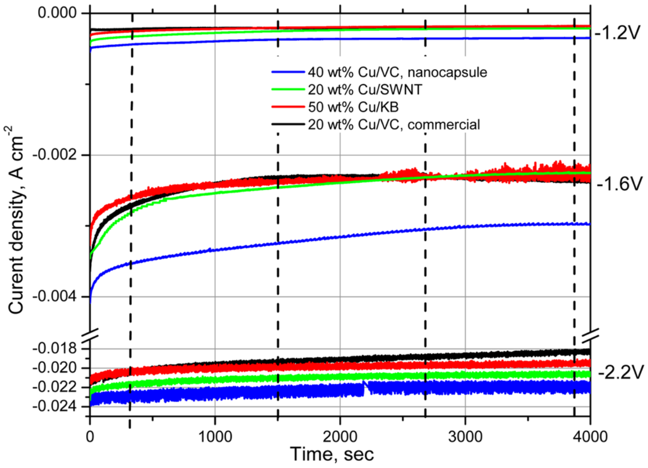

**Figure 4.** Current densities (per geometric surface area) vs time for thin films of 40 wt % Cu/VC (blue), 20 wt % Cu/SWNT (green), 50 wt % Cu/KB (red) and 20 wt % Cu/VC (black) held at −1.2, −1.6, and −2.2 V. $CO_2$-purged 0.1 M $KHCO_3$ solution at pH = 6.8, 1600 rpm, 20 $\mu g_{Cu}\ cm^{-2}$ Cu loading.

It should be noted that in a sealed RDE configuration $CO_2$ reduction products can be quantified from an electrode, having a geometric surface area of just 0.4 $cm^2$, an area more than an order of magnitude smaller than the 6 $cm^2$ electrode reported for electrolysis cells in previous work.[1,40] The cathodic currents in Figure 4 gradually decrease until they level off at ca. 1500 s for all the films held at −1.2 V and ca. 1000 s for the three films (20 wt % Cu/SWNT, 50 wt % Cu/KB, and 40 wt % Cu/VC nanocapsule) held at −2.2 V. For commercial 20 wt % Cu/VC, the current gradually decreases with time. At −1.6 V, the current versus time curve levels off earlier for 50 wt % Cu/KB (ca. 100 s) when compared with the other three films. For the 20 wt % Cu/SWNT and 40 wt % Cu/VC nanocapsule catalyst, the current levels off at ca. 2700 s, whereas for the commercial 20 wt % Cu/VC catalyst, the region of the current decrease (first 2500 s) is followed by a region in which the current remains constant (2500−2700 s) and, finally, another region of current increase (2700−4100 s). Among the four catalysts, the shortest time to reach current plateau is realized using the 50 wt % Cu/KB. The highest cathodic current at constant potential is observed for the 40 wt % Cu/VC catalyst versus the other three catalysts, in agreement with the CV curves shown in Figure 3.

Online gas analysis of $CO_2$ electroreduction products on carbon-supported catalysts was carried out at 300, 1500, 2700, and 3900 s, as shown by the dashed vertical lines in Figure 4. For comparison, the current versus time curves at constant potentials of −1.6, −1.8, −2, and −2.2 V were measured on the films of electrodeposited Cu, as shown in Figure 5. As the holding potential increases from −1.6 to −2.2 V, the current versus time curves shift to more negative currents. However, the current versus time curves for electrodeposited Cu do not plateau in the selected time frames. The current drops with time almost in a linear fashion, with a rate of 0.07, 0.50, 0.35, and 0.29 $\mu$A·sec$^{-1}$ at −1.6, −1.8, −2.0, and −2.2 V, respectively. Overall, the current drops by 21% over 4000 s at −2.2 V, indicating nonstationary processes occurring on the electrode surface. This current instability may be caused by the adsorption of liquid reaction products generated during the $CO_2$ electroreduction on the Cu surface. To avoid significant current variations over the course of the $CO_2$ electroreduction experiment, sampling of the gas mixture for GC analysis was performed at 300 and 1500 s only, so that the current variation would not exceed 10%.

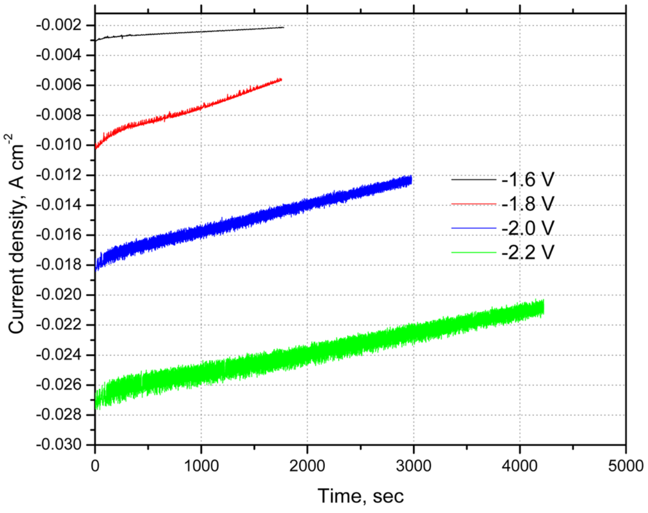

**Figure 5.** Current densities (per geometric surface area) vs time for thin films of electrodeposited Cu. $CO_2$-purged 0.1 M $KHCO_3$ solution at pH = 6.8, 1600 rpm.

Two major differences between the films of electrodeposited Cu and supported Cu nanoparticles are (1) Cu surface structure (polycrystalline vs nanoparticles) and (2) the presence of a carbon support. An important question is whether the support (VC, KB and SWNT) shows electrochemical activity toward the HER and $CO_2$ electroreduction in the potential region from −1.2 to −2.2 V. Current versus time curves for VC, SWNT and KB supports measured at −1.2, −1.6, and −2.2 V are compared to those of 20 wt % Cu/VC, 40 wt % Cu/VC, 20 wt % Cu/SWNT, and 50 wt % Cu/KB in Figure 6a−c (dashed and solid curves, respectively). All three supports show electroreduction activity in $CO_2$-purged 0.1 M

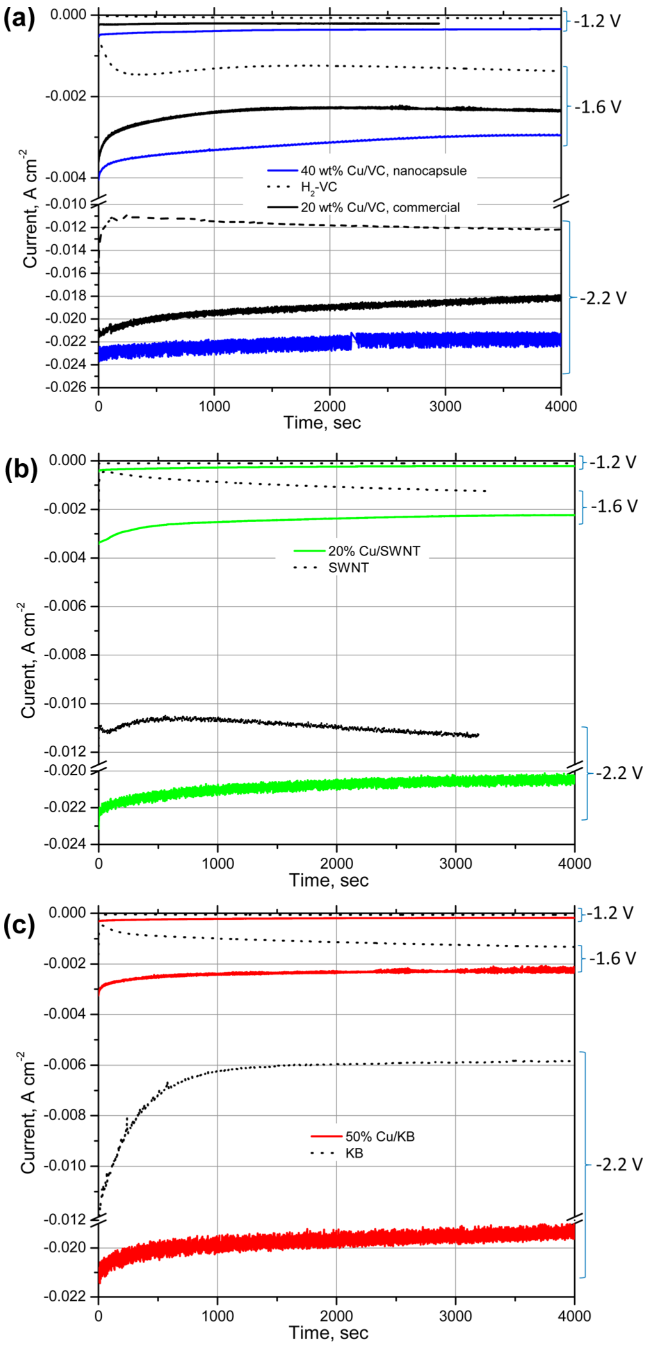

**Figure 6.** Current densities (per geometric surface area) vs time for (a) thin films of 40 wt % Cu/VC (blue) and 20 wt % Cu/VC (black) vs VC (dashed lines); (b) thin films of 20 wt % Cu/SWNT vs SWNT; and (c) thin films of 50 wt % Cu/KB vs KB. Thin films are held at −1.2, −1.6, and −2.2 V. $CO_2$-purged 0.1 M $KHCO_3$ solutions at pH = 6.8, 1600 rpm, 20 $\mu g_{Cu}$ cm$^{-2}$ Cu loading for thin films of 20 wt % Cu/VC, 40 wt % Cu/VC, 20 wt % Cu/SWNT, and 50 wt % Cu/KB. Loadings of thin films of VC, SWNT and KB are 80 $\mu g_{VC}$ cm$^{-2}$, 80 $\mu g_{SWNT}$ cm$^{-2}$, and 20 $\mu g_{KB}$ cm$^{-2}$, respectively.

KHCO$_3$ solution. The current magnitude for VC is ca. half of that for 20 wt % Cu/VC (dashed and solid black curves in Figure 6a, respectively) and less than half of that for 40 wt % Cu/VC (blue lines in Figure 6a) at −1.2 and −1.6 V. The currents at −1.6 and −2.2 V on VC support first decline, but then gradually increase with time. The same trend is observed for the SWNT support (dashed lines in Figure 6 b). However, the current increase with time at −1.6 V is more pronounced for SWNT versus VC, and the SWNT curve approaches the 20 wt % Cu/SWNT curve (green lines in Figure 6b) faster than that for 20 wt % Cu/VC versus VC in Figure 6a. For KB support (dashed lines in Figure 6c), the current gradually increases with time at −1.6 V, but decreases with time at −2.2 V, contrary to other catalysts.

The current variation with time is determined by a variation with time of partial currents for products of the CO$_2$ electroreduction reaction and HER in liquid (not analyzed in this work) and gas phase (i.e., CO, CH$_4$, C$_2$H$_4$, and H$_2$). Partial currents of H$_2$ evolution versus time (as determined by GC analysis) for the four carbon-supported Cu catalysts versus those of corresponding supports at −1.2 V are shown in Figure 7. At times longer than 25 min, the fractions of molecular hydrogen generated by supports (a ratio of H$_2$ partial current produced by the support to that of the corresponding catalyst) are ~30% for both 20 wt % Cu/VC and 50 wt % Cu/KB. For 20 wt % Cu/SWNT and 40 wt % Cu/VC, the supports generate ~40% and 20% H$_2$, respectively. This means that the majority of H$_2$ on the supported catalysts are generated by Cu nanoparticles. The higher fraction of H$_2$ generated by the SWNT support (40%) versus VC and KB supports is due to a higher electrocatalytic activity of SWNTs toward the HER.

At −1.2 V, the three supports generate only hydrogen (not shown in the figure), whereas the supported catalysts generate both H$_2$ and CO. At −1.6 V, the three supports generate both H$_2$ and CO. However, fractions of CO generated by VC, KB, and SWNTs supports are negligible compared to those of corresponding supported Cu catalysts. Generation of CO and CH$_4$ by VC, KB, and SWNTs supports becomes more pronounced at −2.2 V.

Results of online GC analysis in terms of CO and H$_2$ Faradaic efficiencies for the four supported catalysts at −1.2 V are shown in Figure 8. For all the catalysts, the Faradaic efficiency for H$_2$ (solid squares) generation increases with time, although the Faradaic efficiency for CO (open squares) production decreases with time. The 40 wt % Cu/VC generates the greatest amount of CO and the least amount of H$_2$ versus the other catalysts, whereas 20 wt % Cu/VC generates the least amount of CO and the greatest amount of H$_2$ (at times longer than 25 min). The Faradaic efficiencies of 20 wt % Cu/SWNT and 50 wt % Cu/KB for both CO and H$_2$ overlap. At times longer than 45 min, Faradaic efficiencies for all the catalysts level off (within experimental error), implying that stationary processes become predominant on the surface of the supported catalysts. The total Faradaic efficiencies for H$_2$ + CO for 20 wt % Cu/SWNT and 50 wt % Cu/KB are close to 100%, suggesting that no liquid reaction products are generated during CO$_2$ electroreduction at −1.2 V. At −1.4 V, H$_2$ and CO were also the only CO$_2$ electroreduction products, detected in the gas phase.

Hydrocarbon generation was first observed at −1.6 V, with substantial amounts of CH$_4$ and C$_2$H$_4$ detected at more negative potentials. The question may arise whether the stability of thin-film electrodes under potentials, at which substantial amounts of CH$_4$ and C$_2$H$_4$ are generated is affected by adsorption of hydrocarbons. Faradaic efficiencies of 40 wt % Cu/VC, 20 wt % Cu/SWNT, 50 wt % Cu/KB, and commercial 20 wt % Cu/VC toward CH$_4$, C$_2$H$_4$, CO, and H$_2$ generation at −2 V as a function of time are shown in Figure 9a−d, respectively. For all four catalysts, the level of CO produced is below 5%, and it is fairly stable with time. Faradaic efficiencies for C$_2$H$_4$ and CH$_4$ generation on thin films of 40 wt % Cu/VC, 20 wt % Cu/SWNT, and 50 wt % Cu/KB follow the same pattern: they increase between 5 and 25 min and then level off or slightly decrease with time as in the case of 40 wt % Cu/VC (Figure 9a). An increase in Faradaic efficiencies for CH$_4$ and C$_2$H$_4$ formation between 5 and 25 min is accompanied by a decrease (Figure 9c) or stable response (Figure 9a,b) with respect to H$_2$ formation. At times longer than 25 min, H$_2$ Faradaic efficiencies increase with time. The arrangement of CH$_4$ and C$_2$H$_4$ curves is significantly different for the commercial 20 wt % Cu/VC, whereas C$_2$H$_4$ generation is dominated by CH$_4$ in the beginning of the experiment (at 5

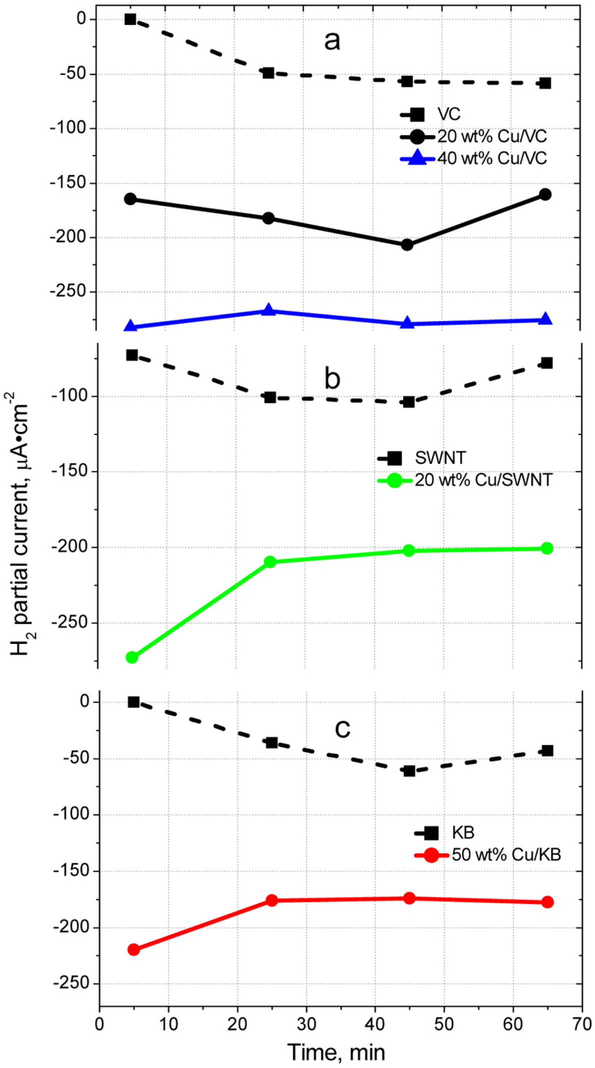

**Figure 7.** H$_2$ partial currents vs time curves for supported Cu catalysts (solid lines and symbols) vs corresponding supports (black dashed lines and solid square symbols) held at −1.2 V: (a) 40 wt % Cu/VC (blue triangles), 20 wt % Cu/VC (black solid circles), and VC support; (b) 20 wt % Cu/SWNT (green sold circles) and SWNT support; and (c) 50 wt % Cu/KB (solid red circles) and KB support.

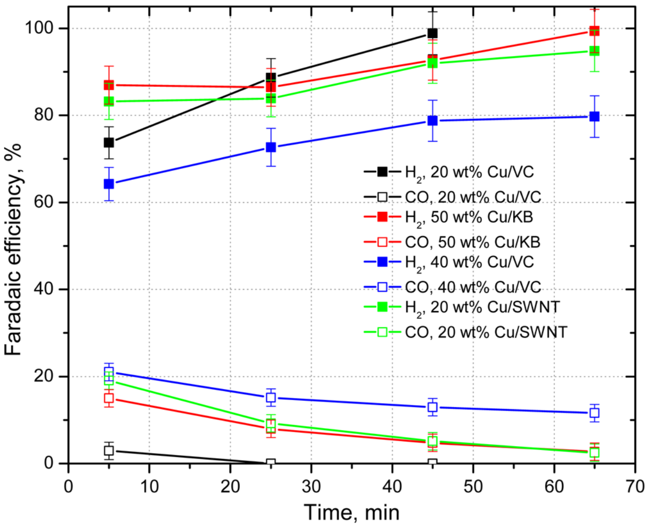

**Figure 8.** Faradaic efficiencies vs time for $H_2$ (solid squares) and CO (open squares) generation at thin films of 40 wt % Cu/VC (blue), 20 wt % Cu/SWNT (green), 50 wt % Cu/KB (red), 20 wt % Cu/VC (black), and 20 wt % Cu/VC (black) held at −1.2 V. $CO_2$-purged 0.1 M $KHCO_3$ solutions at pH = 6.8, 1600 rpm, 20 $\mu g_{Cu}$ $cm^{-2}$ Cu loading.

min), their order changes at times longer than 25 min. $H_2$ Faradaic efficiency steadily increases with time for this catalyst. Total Faradaic efficiency ($H_2$ + CO + $CH_4$ + $C_2H_4$) increases between 5 and 25 min and then approaches 90−100% for all the catalysts. Although it is difficult to comment on the reasons behind different patterns of stability for different catalysts, the promising feature of Figure 9 is that Faradaic efficiencies for $CH_4$ and $C_2H_4$ generation on 40 wt % Cu/VC, 20 wt % Cu/SWNT and 50 wt % Cu/KB do not change significantly with time, despite changes on the surface as indicated by the increase in Faradaic efficiency for $H_2$ production.

Figure 10 shows the Faradaic efficiencies for $H_2$, CO, $CH_4$, and $C_2H_4$ as well as the total Faradaic efficiency ($H_2$ + CO + $CH_4$ + $C_2H_4$) versus potential for 40 wt % Cu/VC (a), commercial 20 wt % Cu/SWNT (b), 50 wt % Cu/KB (c), 40 wt % Cu/VC (d), and electrodeposited Cu (e). The common features of the graphs presented in Figure 10a−d are as follows: (1) the $H_2$ Faradaic efficiency starts declining from the 80−90% level as CO begins to generate at −1.2 V and continues declining to the 10−20% level at −2.2 V; (2) the CO Faradaic efficiency passes through a maximum near −1.6 V; (3) a decline in the CO Faradaic efficiency to the left of the maximum is accompanied by an increase in the $CH_4$ and $C_2H_4$ Faradaic efficiencies due to CO consumption in the process of $CH_4$ and $C_2H_4$ generation.[4,18] At −2.2 V, CO Faradaic efficiency becomes negligible for all the supported catalysts, indicating that all of the CO is consumed in the production of $CH_4$ and $C_2H_4$. At the same time, in the potential range between −2.0 and −2.2 V the Faradaic efficiencies for $CH_4$ and $C_2H_4$ generation begin to level off, likely because generation of $CH_4$ and $C_2H_4$ becomes limited by the rate of CO generation. The three trends listed above are consistent with the previously reported results for polycrystalline Cu.[4,18] It should be mentioned that the potential range for hydrocarbon formation on electrodeposited Cu is more narrow (Figure 10e). It covers only 0.6 V (from −1.6 to −2.2 V) versus 0.8 V (from −1.4 to −2.2 V) for supported Cu nanoparticles (Figures 10a−d). The supported catalysts can be divided into two groups based on the ratio of Faradaic efficiencies for $CH_4$ to $C_2H_4$ and onset potentials for the generation of $CH_4$ and $C_2H_4$. For more agglomerated 20 wt % Cu/VC (Figure 10d) and 50 wt % Cu/KB (Figure 10c), onset potentials for $CH_4$ and $C_2H_4$ generation

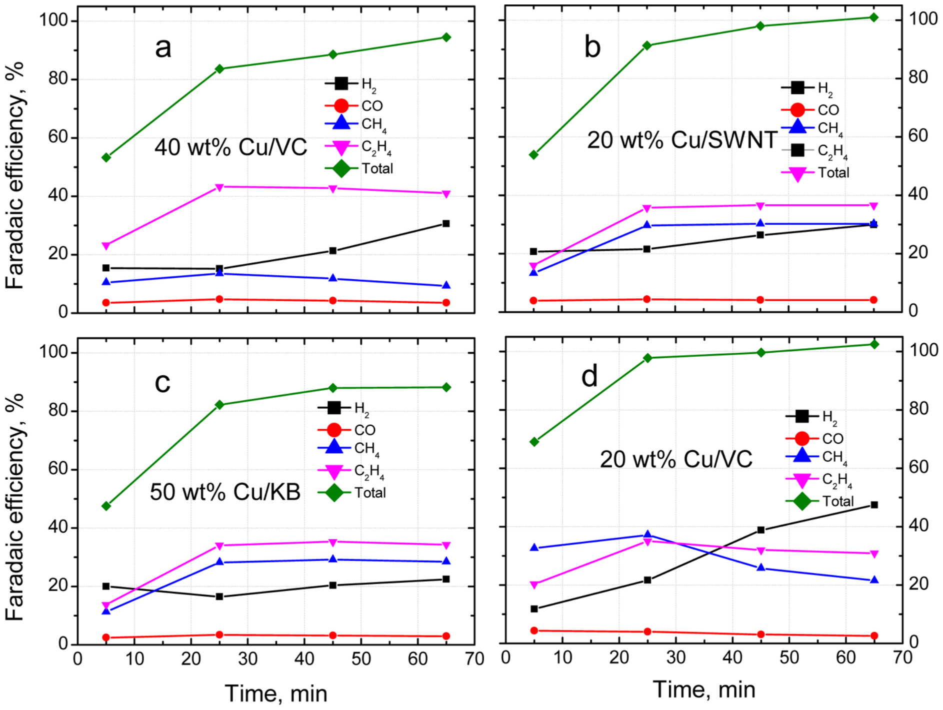

**Figure 9.** Faradaic efficiencies vs time for $H_2$ (solid black squares), CO (solid red circles), $CH_4$ (solid blue triangles), and $C_2H_4$ (magenta solid upside down triangles) generation at thin films of (a) 40 wt % Cu/VC, (b) 20 wt % Cu/SWNT, (c) 50 wt % Cu/KB, and (d) 20 wt % Cu/VC held at −2.0 V. $CO_2$-purged 0.1 M $KHCO_3$ solutions at pH = 6.8, 1600 rpm, 20 $\mu g_{Cu}$ $cm^{-2}$ Cu loading. Green diamonds—total Faradaic efficiencies for $H_2$, CO, $CH_4$, and $C_2H_4$ generation.

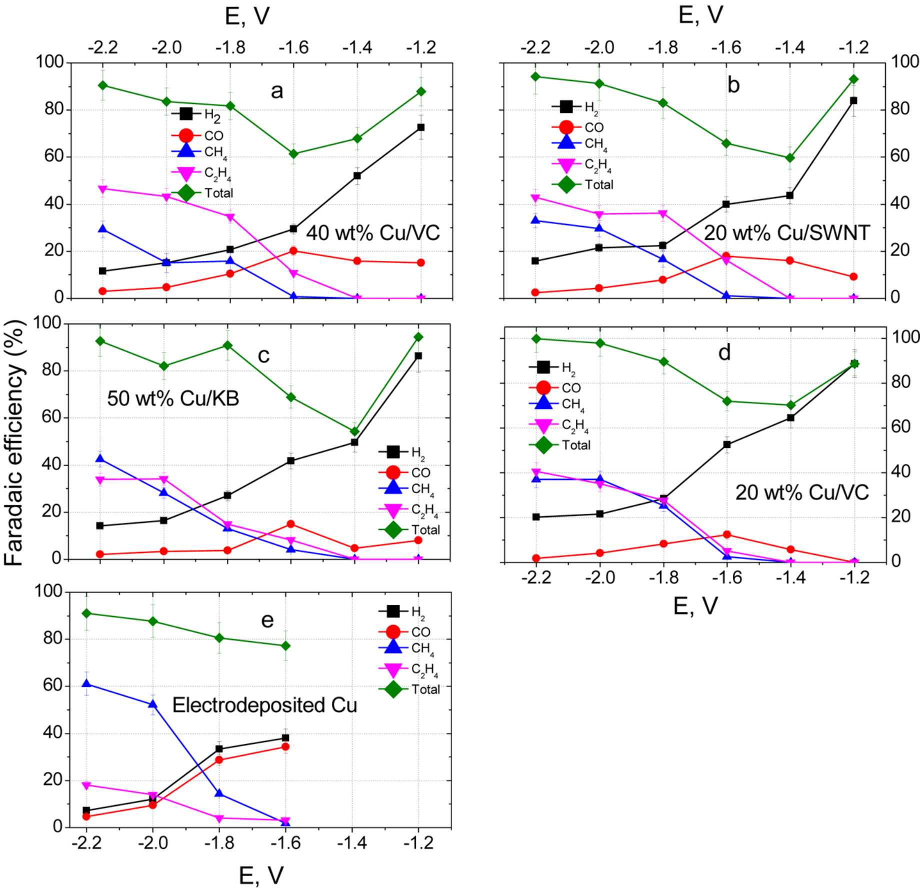

**Figure 10.** Faradaic efficiencies vs potential for $H_2$ (solid black squares), CO (solid red circles), $CH_4$ (solid blue triangles), and $C_2H_4$ (magenta solid upside down triangles) generation at thin films of (a) 40 wt % Cu/VC, (b) 20 wt % Cu/SWNT, (c) 50 wt % Cu/KB, (d) 20 wt % Cu/VC, and (e) electrodeposited Cu. Green diamonds—total Faradaic efficiencies for $H_2$, CO, $CH_4$ and $C_2H_4$ generation. $CO_2$-purged 0.1 M $KHCO_3$ solutions at pH = 6.8, 1600 rpm, 20 $\mu g_{Cu}$ cm$^{-2}$ Cu loading for supported catalysts. GC sampling is performed at 25 min.

are identical (−1.4 V), as well as magnitude of Faradaic efficiencies for $CO_2$ conversion into $CH_4$ and $C_2H_4$. For the two catalysts with better-dispersed Cu nanoparticles, that is, 40 wt % Cu/VC (Figure 10a) and 20 wt % Cu/SWNT (Figure 10b), $C_2H_4$ is generated at lower potentials than $CH_4$ (−1.4 vs −1.6 V), and the Faradaic efficiencies for $C_2H_4$ production exceed those of $CH_4$ production. Given that the average size of the Cu nanoparticles in 20 wt % Cu/SWNT and 40 wt % Cu/VC catalysts is 19 and 12 nm, respectively, a preliminary conclusion might be drawn that the smaller the size of the Cu nanoparticles, the larger is the ratio of Faradaic efficiencies for $C_2H_4$ to $CH_4$. The larger ratio of $C_2H_4$/$CH_4$ Faradaic efficiencies in 40 wt % Cu/VC catalyst versus 20 wt % Cu/SWNT catalyst might also be due to the effect of the support. However, a larger ratio of $C_2H_4$/$CH_4$ Faradaic efficiencies is also observed for 40 wt % Cu/VC versus 20 wt % Cu/VC (i.e., two catalysts with the same support) but with different particle sizes (12 nm vs 27 nm, respectively).

There is a significant difference in the $CH_4$ and $C_2H_4$ distribution for more agglomerated Cu nanoparticles in 50 wt % Cu/KB and 20 wt % Cu/VC (Figure 10c,d, respectively) versus electrodeposited Cu in Figure 10e. For the electrodeposited Cu electrode, Faradaic efficiency for $CH_4$ at −2.2 V (60%) is three times higher than that of $C_2H_4$ (19%).

Total Faradaic efficiencies in Figure 10a−e (green lines and diamonds) that include Faradaic efficiencies of all the detected gas-phase reaction products ($H_2$, CO, $CH_4$ and $C_2H_4$) follow the same trend: a relatively flat area between −2.0 and −2.2 V is followed by a drop between −1.4 and −1.6 V (for carbon-supported catalysts), and an increase between −1.2 and −1.4 V. The drop in Faradaic efficiencies between −1.4 and −1.6 V is likely due to the generation of liquid $CO_2$ electroreduction products such as HCOOH, $C_2H_5OH$ and $C_3H_7OH$,[4,5] while high total Faradaic efficiencies (within 80−100%) from the left and right of the minimum indicate, that in these potential regions, mostly gas-phase reaction products are generated, with $CH_4$ and $C_2H_4$ being the greatest contributors to the total Faradaic efficiency at potentials more negative than −1.6 V.

In summary, significant difference in the $CO_2$ reduction product distribution were observed between the electrodeposited Cu and the supported Cu catalysts. $CH_4$ and $C_2H_4$ are generated at lower potentials on supported Cu catalysts versus electrodeposited Cu. Appreciable Faradaic efficiencies for $CH_4$ and $C_2H_4$ are observed at potentials more negative than −1.6 V and −1.8 V for supported Cu catalysts and electrodeposited Cu, respectively. The onset potential for $C_2H_4$ generation is also shifted by 0.2 V (from −1.6 to −1.4 V, see Figure 10) for the supported Cu nanoparticles versus smooth Cu films, implying that the overpotential of $CO_2$ electroreduction reaction to $C_2H_4$ can be reduced by 200 mV by switching from smooth Cu films to Cu nanoparticles. Although the product distribution is strongly dominated by $CH_4$ over $C_2H_4$ (a factor of 3 at −2.0 V) for electrodeposited Cu, the Faradaic efficiencies for $CH_4$ and $C_2H_4$ are almost the same for agglomerated Cu nanoparticles supported on KB and VC (Figure 10c,d, respectively). For 40 wt % Cu/VC (Figure 9a) and 20 wt % Cu/SWNT (Figure 10b), the Faradaic efficiency for $C_2H_4$ dominates over that of $CH_4$. This dominance of $C_2H_4$ over $CH_4$ becomes more pronounced as the particles become smaller, that is, the ratio of Faradaic efficiencies for $C_2H_4/CH_4$ is larger for 40 wt % Cu/VC with 12 nm particle size (2.0 at −2.0 V) versus 20 wt % Cu/SWNT with 19 nm particle size (1.3 at −2.0 V). This trend is consistent with observations reported by several research groups for surfaces with different morphology[6,7] and theoretically justified in ref.[7] Rough surfaces (containing corners, edges, and defects) are found to be more active toward $C_2H_4$ production than smooth surfaces (like electrodeposited Cu). As such, the more corners and edges or the smaller the particle size, the higher the Faradaic efficiencies are expected toward $C_2H_4$ production. A similar behavior was reported by Gonsalves et al.[8] for Cu electrodeposits with different morphology and, consequently, different roughness. At −1.9 V versus Ag/AgCl, for a smooth electropolished Cu mesh catalyst the product distribution was dominated by $CH_4$, whereas the product distribution was dominated by $C_2H_4$ for rough dendritic structures.

The main difference between $CO_2$ reduction on the rough electrodeposited Cu surfaces in ref 8 and the carbon-supported Cu nanoparticles in our work is Faradaic efficiencies for $CH_4$ generation. At −1.9 V, Faradaic efficiencies for $CH_4$ generation are within 20−30% for carbon-supported Cu catalysts in our work (see Figure 10), although it is less than 3% for copper electrodeposits investigated by Gonsalves et al.[8] This difference is likely due to contribution from molecular hydrogen generated by carbon supports at these negative potentials. Excess hydrogen may push the $CO_2$ electroreduction reaction toward $CH_4$ generation.[4,41] Correlation between hydrogen evolution and methane formation on polycrystalline Cu was first established by Hori[4] and has been recently confirmed for $CO_2$ electroreduction on Cu(100) at very low and high pH.[41] Methane formation as a function of potential was closely followed by generation of molecular hydrogen, although no such correlation was observed for $C_2H_4$. The mechanism for the influence of adsorbed hydrogen on methane generation was proposed by Gattrell et al.,[3] although it has never been confirmed experimentally.

The consumption of $H_2$ generated by VC, KB and SWNT supports during $CO_2$ electroreduction to hydrocarbons on thin films of 40 wt % Cu/VC, 50 wt % Cu/KB, 20 wt % Cu/SWNT and 20 wt % Cu/VC at −1.6 and −2.2 V is illustrated in Figure 11. At −1.2 V, when no hydrocarbons are produced by Cu nanoparticles, the VC, KB and SWNT supports produce much less hydrogen than the corresponding supported Cu catalysts. The ratio of $H_2$ partial currents generated by the supported catalyst to the corresponding support varies from 2 for 20 wt % Cu/SWNT to 5.4 for 40 wt % Cu/VC. On the contrary, at more negative potentials of −1.6 and −2.2 V, at which $CH_4$ and $C_2H_4$ are detected by GC analysis, the supported catalyst-to-support ratios of $H_2$ partial currents suddenly drop. These ratios vary between 0.73 (40 wt % Cu/VC and 20 wt % Cu/SWNT) and 0.90 (20 wt % Cu/VC) at −1.6 V and 0.4 (20 wt % Cu/SWNT) and 1.2 (20 wt % Cu/VC) at −2.2 V, suggesting lower (or slightly higher) $H_2$ partial currents generated by the supported catalysts (i.e., catalyst + support) versus those of corresponding supports. This can be true only if part of $H_2$ generated by VC, KB, and SWNT supports is consumed during $CO_2$ electroreduction to hydrocarbons likely due to hydrogen spillover. Although the promotion of methane generation by hydrogen on the Cu surface has been reported before,[4,41] it has never been reported for the supported Cu surfaces at which the molecular hydrogen is generated from a surface other than a Cu surface.

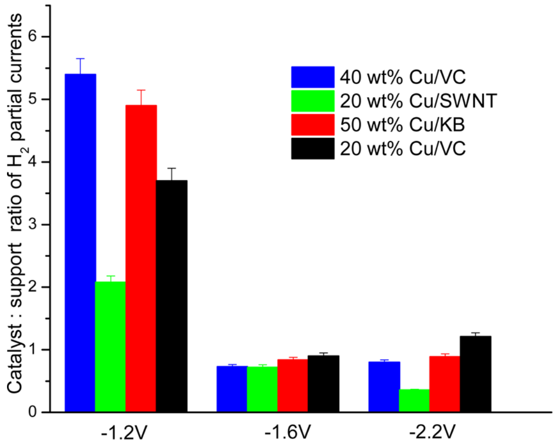

**Figure 11.** Supported catalyst-to-support ratios of $H_2$ partial currents calculated for thin films of 40 wt % Cu/VC (blue), 20 wt % Cu/SWNT (green), 50 wt % Cu/KB (red), and 20 wt % Cu/VC (black) at −1.2, −1.6, and −2.2 V. GC sampling is performed at 25 min.

The lower activity of the electrodeposited smooth Cu films for hydrocarbon formation versus supported catalysts at potentiostatic conditions is consistent with more negative onset potential of the plateau (−1.28 V) on the $CO_2$ reduction curve shown in Figure 3 (orange curve). As mentioned above, the plateau was assigned by Hori[4,38] to the inhibition of hydrogen evolution by adsorbed CO molecules. As such, the more negative onset potential of the plateau would indicate lower activity toward CO generation for electrodeposited Cu films versus that of the supported nanoparticles and, therefore, lower activity toward hydrocarbon generation, as CO is a key intermediate toward the production of $CH_4$ and $C_2H_4$.[4] Interestingly, the presence and absence of the shoulders for the four carbon-supported catalysts in Figure 3 correlates fairly well with their Faradaic efficiencies toward CO and $H_2$ generation at −1.2 V, as shown in Figure 8. For the commercial 20 wt % Cu/VC (black curve in Figure 3), no shoulder is observed in the vicinity of −1.25 V, and the Faradaic efficiency toward CO generation at −1.2 V is negligible (below 3%, open black squares in Figure 8). This implies that the majority of the current near −1.2 V is due to $H_2$ generation. For the other three samples, the Faradaic efficiencies toward CO generation are significantly higher (15−20% at 5 min in Figure 8) than that of 20 wt % Cu/VC, and well-pronounced plateaus in the vicinity of −1.25 V are evident. The differences in the magnitude of current in the vicinity of the plateau region for 40 wt % Cu/VC (blue curve), 20 wt % Cu/SWNT (green curve), 50 wt % Cu/KB (red curve), and 20 wt % Cu/VC (black line) reflect the difference in their Cu ECSA (see Table 1), as well as some other factors such as double layer charging for 20 wt % Cu/SWNT, $CO_2$ reduction to formate ions[4] and differences in morphology of nanoparticles.[39]

Note that our preliminary conclusion on particle size effect for 10−30 nm supported Cu nanoparticles is not consistent with the predicted trend for a product selectivity recently proposed by Reske et al.[42] In their experiments, particle size effect was explored for 2−15 nm unsupported Cu nanoparticles. Catalytic activities of 2−15 nm Cu nanoparticles held at −1.1 V versus RHE toward the $CO_2$ electroreduction were significantly affected by particle size. For particles smaller than 5 nm, significant increase in activities toward $H_2$ and CO generation was accompanied by a slight increase in $CH_4$ and decrease in $C_2H_4$ generation. The product distribution was strongly dominated by $H_2$ (65% Faradaic selectivity) and CO (ca. 25% Faradaic selectivity), while Faradaic selectivities for $CH_4$ and $C_2H_4$ were significantly lower (12 and 3%, respectively). Almost no particle size effect on selectivity was observed, except the region below 2 nm, in which selectivity toward CO production dropped to zero. Increased selectivities for $H_2$ and CO generation for 2−15 nm nanoparticles were interpreted in terms of strong chemisorption of $H_2$ and CO to low-coordinated nanoparticle sites. For particles larger than 15 nm, the authors predict a monotonic decrease in $H_2$ and CO selectivities, accompanied by an increase in selectivites for $C_2H_4$ and $CH_4$ generation. Product distribution is expected to be dominated by $CH_4$ over $C_2H_4$.

In similar experimental conditions (−1.1 V vs RHE or ca. −1.7 V vs Ag/AgCl), we observe similar Faradaic efficiencies for $H_2$ and $C_2H_4$ (22−25%) and CO and $CH_4$ (ca. 13%) generation both for 12 nm (40 wt % Cu/VC, Figure 10a) and 19 nm (20 wt % Cu/SWNT, Figure 10b) Cu nanoparticles (i.e., the product distribution is dominated by $C_2H_4$ over $CH_4$). An explanation for the inconsistency between product selectivities in our work versus those observed and predicted by Reske et al.[42] might be higher agglomeration of Cu nanoparticles resulting either from the heat-treatment (for 40 wt % Cu/VC) or using aqueous solvent in synthesis (for 20 wt % Cu/SWNT). The higher agglomeration gives a surface structure which is different from the structure of ideal cubooctahedral nanoparticles of a given size. A more detailed study would be required in order to draw a final conclusion on the effect of Cu particle size on product selectivity for 10−30 nm nanoparticles.

## CONCLUSIONS

1. Various 10−30 nm Cu nanoparticles supported on VC, KB, and SWNTs were synthesized using different synthetic routes. We found that larger and more agglomerated Cu particles are formed if water is present during the Cu reduction step. Better-dispersed, smaller (ca. 12 nm) nanoparticles are obtained in the presence of a nonaqueous, nonpolar solvent such as oleylamine that act as both the solvent and surfactant. Cu nanoparticles supported on nanostructured SWNTs appear to be less susceptive to oxidation in air and agglomeration during reductive treatment in $H_2$ compared to other catalysts.
2. Carbon-supported Cu nanocatalysts are more selective toward $C_2H_4$ generation versus electrodeposited Cu, in agreement with previously reported results for unsupported 50−100 nm nanoparticles.[7] Contrary to previous results reported for 50−100 nm unsupported Cu nanoparticles,[7] an appreciable amount of $CH_4$ is generated on carbon-supported Cu nanoparticles at potentials more negative than −1.6 V. Promotion of $CH_4$ generation is assigned to hydrogen spillover from the VC, SWNT, and KB supports that become active toward the HER at potentials more negative than −1.2 V.
3. For the well-dispersed 40 wt % Cu/VC (ca. 12 nm) and 20 wt % Cu/SWNT (ca. 19 nm) catalysts, there is a significant (ca. 200 mV) shift in onset potentials for $C_2H_4$ generation versus electrodeposited Cu, indicating their higher activity toward $C_2H_4$ generation. The ratio of $C_2H_4/CH_4$ Faradaic efficiencies is believed to decrease with a decrease in Cu particle size, likely due to an increase in the number of low-coordination sites, such as corners, edges, and defects.
4. A sealed RDE setup was designed and tested for online analysis of $CO_2$ reduction products in gas phase by GC. Here, we demonstrate that using the RDE setup in a sealed configuration allows the collection of a reproducible GC signal from electrodes with ca. an order of magnitude lower surface area compared to that of electrolysis cells (0.4 vs 6 $cm^2$). Future effort will compare specific activities of nanoparticles toward $CO_2$ electroreduction after thin-film optimization is performed.

## ASSOCIATED CONTENT

### Supporting Information

Elemental composition and Cu and carbon speciation for 40 wt % Cu/VC, 20 wt % Cu/SWNT, 50 wt % Cu/KB, and 20 wt % Cu/VC before and after reduction by 10 vol % $H_2$ in $N_2$ based on XPS analysis from the C-1s, Cu-2p, and O-1s regions. This material is available free of charge via the Internet at http://pubs.acs.org.

## AUTHOR INFORMATION

### Corresponding Author

*E-mail: olga.baturina@nrl.navy.mil.

### Notes

The authors declare no competing financial interest.

## ACKNOWLEDGMENTS

We are grateful to Dr. Karen Swider-Lyons for discussions of this work. Financial support for this work was provided by the Office of Naval Research. Monica Padilla's 2012 summer internship at NRL was supported by NRL HBCU/MITCU program. W. Li is grateful to the financial support from the National Science Foundation (Award No. CBET1235982).

## REFERENCES

(1) Hori, Y. In *Modern Aspects of Electrochemistry*; Vayenas, C. G., White, R. E., Gamboa-Aldeco, M. E., Eds.; Springer: New York, 2008; Vol. *42*.

(2) Gasteiger, H. A.; Kocha, S. S.; Sompalli, B.; Wagner, F. T. *Appl. Catal., B* **2005**, *56*, 9−35.

(3) Gattrell, M.; Gupta, N.; Co, A. *J. Electroanal. Chem.* **2006**, *594*, 1−19.

(4) Hori, Y.; Murata, A.; Takahashi, R. *J. Chem. Soc., Faraday Trans. 1* **1989**, *85*, 2309−2326.

(5) Hori, Y.; Takahashi, I.; Koga, O.; Hoshi, N. *J. Phys. Chem. B* **2002**, *106*, 15−17.

(6) Hori, Y.; Takahashi, I.; Koga, O.; Hoshi, N. *J. Mol. Catal. A: Chem.* **2003**, *199*, 39−47.

(7) Tang, W.; Peterson, A. A.; Varela, A. S.; Jovanov, Z. P.; Bech, L.; Durand, W. J.; Dahl, S.; Norskov, J. K.; Chorkendorff, I. *Phys. Chem. Chem. Phys.* **2012**, *14*, 76−81.

(8) Goncalves, M. R.; Gomes, A.; Condeco, J.; Fernandes, T. R. C.; Pardal, T.; Sequeira, C. A. C.; Branco, J. B. *Electrochim. Acta* **2013**, *102*, 388−392.

(9) Frese, K. W., Jr. *Electrochemical and Electrocatalytic Reactions of Carbon Dioxide*; Elsevier: Amsterdam, 1993.

(10) Shibata, H.; Moulijn, J. A.; Mul, G. *Catal. Lett.* **2008**, *123*, 186−192.

(11) Momose, Y.; Sato, K.; Ohno, O. *Surf. Interface Anal.* **2002**, *34*, 615−618.

(12) Koga, O.; Nakama, K.; Murata, A.; Hori, Y. *Denki Kagaku* **1989**, *57*, 1137−1140.

(13) Perez-Cadenas, A. F.; Ros, C. H.; Morales-Torres, S.; Perez-Cadenas, M.; Kooyman, P. J.; Moreno-Castilla, C.; Kapteijn, F. *Carbon* **2013**, *56*, 324−331.

(14) Genovese, C.; Ampelli, C.; Perathoner, S.; Centi, G. *J. Catal.* **2013**, *308*, 237−249.

(15) Genovese, C.; Ampelli, C.; Perathoner, S.; Centi, G. *J. Energy Chem.* **2013**, *22*, 202−213.

(16) Dewulf, D. W.; Jin, T.; Bard, A. J. *J. Electrochem. Soc.* **1989**, *136*, 1686−1691.

(17) Schouten, K. J. P.; Kwon, Y.; van der Ham, C. J. M.; Qin, Z.; Koper, M. T. M. *Chem. Sci.* **2011**, *2*, 1902−1909.

(18) Hori, Y.; Murata, A.; Takahashi, R.; Suzuki, S. *J. Am. Chem. Soc.* **1987**, *109*, 5022−5023.

(19) Kim, J. J.; Summers, D. P.; Frese, K. W. *J. Electroanal. Chem.* **1988**, *245*, 223−244.

(20) Cook, R. L.; Macduff, R. C.; Sammells, A. F. *J. Electrochem. Soc.* **1989**, *136*, 1982−1984.

(21) Peterson, A. A.; Abild-Pedersen, F.; Studt, F.; Rossmeisl, J.; Norskov, J. K. *Energy Environ. Sci.* **2010**, *3*, 1311−1315.

(22) Norskov, J.; Peterson, A. *Abstracts of Papers of the American Chemical Society*, 243rd National Meeting of the American Chemical Society, San Diego, CA, March 25−29, 2012, FUEL-5, 2012; American Chemical Society: Washington, DC, 2012.

(23) Damaskin, B. B.; Petrii, O. A. *Introduction into Electrochemical Kinetics*, 2nd ed.; Vysshaya shkola: Moscow, 1983.

(24) Bandi, A.; Kuhne, H. M. *J. Electrochem. Soc.* **1992**, *139*, 1605−1610.

(25) Aoki, A.; Nogami, G. *J. Electrochem. Soc.* **1995**, *142*, 423−427.

(26) Nasirpouri, F. *Ionics* **2011**, *17*, 331−337.

(27) Siegenthaler, H.; Juttner, K. *J. Electroanal. Chem.* **1984**, *163*, 327−343.

(28) Wu, J.; Risalvato, F.; Zhou, X.-D. *Electrochemical Synthesis of Fuels 1* **2012**, *41*, 49−60.

(29) Wu, J.; Risalvato, F. G.; Ke, F.-S.; Pellechia, P. J.; Zhou, X.-D. *J. Electrochem. Soc.* **2012**, *159*, F353−F359.

(30) Chen, Y.; Kanan, M. W. *J. Am. Chem. Soc.* **2012**, *134*, 1986−1989.

(31) Chen, Y.; Li, C. W.; Kanan, M. W. *J. Am. Chem. Soc.* **2012**, *134*, 19969−19972.

(32) Zhang, Z.; More, K. L.; Sun, K.; Wu, Z.; Li, W. *Chem. Mater.* **2011**, *23*, 1570−1577.

(33) Tobias, G.; Shao, L.; Salzmann, C. G.; Huh, Y.; Green, M. L. H. *J. Phys. Chem. B* **2006**, *110*, 22318−22322.

(34) Garsany, Y.; Baturina, O. A.; Swider-Lyons, K. E.; Kocha, S. S. *Anal. Chem.* **2010**, *82*, 6321−6328.

(35) Trasatti, S.; Petrii, O. A. *Pure Appl. Chem.* **1991**, *63*, 711−734.

(36) Baturina, O. A.; Gould, B. D.; Garsany, Y.; Swider-Lyons, K. E. *Electrochim. Acta* **2010**, *55*, 6676−6686.

(37) Machado, S. A. S.; Tanaka, A. A.; Gonzalez, E. R. *Electrochim. Acta* **1994**, *39*, 2591−2597.

(38) Hori, Y.; Murata, A.; Takahashi, R.; Suzuki, S. *J. Chem. Soc. Chem. Commun.* **1988**, 17−19.

(39) Kortlever, R.; Tan, K. H.; Kwon, Y.; Koper, M. T. M. *J. Solid State Electrochem.* **2013**, *17*, 1843−1849.

(40) Popic, J. P.; AvramovIvic, M. L.; Vukovic, N. B. *J. Electroanal. Chem.* **1997**, *421*, 105−110.

(41) Schouten, K. J. P.; Gallent, E. P.; Koper, M. T. M. *J. Electroanal. Chem.* **2014**, *716*, 53−57.

(42) Reske, R.; Mistry, H.; Behafarid, F.; Cuenya, B. R.; Strasser, P. *J. Am. Chem. Soc.* **2014**, *136*, 6978−6986.